UC San Diego
UC San Diego Previously Published Works

Title

Seismic behavior of a partially grouted reinforced masonry structure: Shake-table testing and numerical analyses

Permalink

https://escholarship.org/uc/item/7zh4c9t5

Journal

Earthquake Engineering & Structural Dynamics, 49(11)

ISSN

0098-8847

Authors

Koutras, Andreas A
Shing, P Benson

Publication Date

2020-09-01

DOI

10.1002/eqe.3281

Peer reviewed

WILEY

Seismic behavior of a partially grouted reinforced masonry structure: Shake-table testing and numerical analyses

Andreas A. Koutras 🄳 | P. Benson Shing

Department of Structural Engineering,
University of California, San Diego, La
Jolla, CA, USA

Correspondence
:
Andreas Koutras, Department of
Structural Engineering, University of
California, San Diego, La Jolla, CA, USA.

Email: akoutras@ucsd.edu

Summary

In regions of low to moderate seismicity in North America, reinforced masonry structures are mostly partially grouted. The behavior of such structures under lateral seismic loads is complicated because of the interaction of the grouted and ungrouted masonry. As revealed in past experimental studies, the performance of partially grouted masonry (PGM) walls under in-plane cyclic lateral loading is inferior to that of fully grouted walls. However, the dynamic behavior of a PGM wall system under severe seismic loads is not well understood. In this study, a full-scale, one-story, PGM building designed for a moderate seismic zone according to current code provisions was tested on a shake table. It was shown that the structure was able to develop an adequate base shear capacity and withstand two earthquake motions that had an effective intensity of two times the maximum considered earthquake with only moderate cracking in mortar joints. However, the structure eventually failed in a brittle manner in a subsequent motion that had a slightly lower effective intensity. A detailed finite element model of the test structure has been developed and validated. The model has been used to understand the distribution of the lateral force resistance among the wall components and to evaluate the shear-strength equation given in the design code. The code equation has been found to be adequate for this structure. Furthermore, a parametric study conducted with the finite element model has shown that the introduction of a continuous bond beam right below a window opening is highly beneficial.

KEYWORDS

earthquake loading, nonlinear finite element analysis, partial grouting, reinforced masonry, shake-table testing, shear-dominated behavior

1 | INTRODUCTION

Reinforced masonry (RM) is commonly used in North America and other regions for low-rise residential, commercial, and school buildings. In these structures, RM shear walls are the primary elements resisting lateral earthquake or wind loads and gravity loads. In modern practice, RM walls are generally constructed of hollow concrete masonry units. Steel reinforcing bars are placed within the units in continuous vertical cells and horizontal courses. RM walls can be either fully or partially grouted. In a partially grouted wall, only the reinforced vertical cells and reinforced horizontal courses (bond beams) are grouted. Partially grouted masonry (PGM) walls may also have reinforcement in the form of steel wire (joint reinforcement) embedded in mortar bed joints to serve as shear reinforcement or to satisfy the prescriptive

requirement of the code. Design provisions for RM in the United States are provided in TMS 402.[1] Although the code does not prohibit the use of PGM in areas of high seismicity, PGM is mainly and predominantly used in areas of low to moderate seismicity, where the code permits larger spacing of the vertical and horizontal reinforced cells. Walls with reinforcing bars spaced at 1.2 to 3.0 m (4 to 10 ft) are classified as ordinary walls and are permitted to be used for Seismic Design Categories (SDC) A, B, and C, as defined in ASCE/SEI 7-16.[2] Such walls are not required to abide by the shear capacity-design provisions of TMS 402 and are thus more prone to shear-dominated behavior.

While a number of studies have been carried out to investigate the seismic performance of fully grouted RM structures, far less attention has been devoted to PGM, although the latter constitutes the vast majority of the RM construction outside the West Coast, in North America. Understanding and predicting the seismic behavior of PGM are challenging due to its inherent heterogeneity and the interaction between the grouted and ungrouted parts. To evaluate the safety of such construction for a moderate seismic zone in the United States, Clough et al[3] conducted shake-table tests on light-roof, single-story, PGM houses. They concluded that such construction could meet the safety standard of the then current code (1976 UBC). Recent experimental studies have shown that the behavior and failure modes of PGM walls strongly depend on the spacing of the grouted cells. When the spacing is large (over 1.2 m), PGM walls tend to exhibit a behavior similar to RC infilled frames.[4] The PGM walls tested by Minaie et al,[4] which had vertical grouted cells spaced at 1.2 m (4 ft), revealed that the shear-strength equation in the then design code (MSJC 2010) could overestimate their shear strength by a factor of 2. To address this issue, a strength-reduction factor of 0.75 was introduced in the shear-strength equation in the 2013 edition of TMS 402. Nolph and ElGawady[5] tested shear-dominated PGM walls to investigate the influence of the spacing of the vertical grouted cells and of the amount of horizontal reinforcement on the shear capacity of the walls. They studied walls that had only one bond beam, which was located at the mid-height, and vertical grouted cells with spacings of 0.6 m (2 ft), 0.8 m (2.6 ft), and 1.2 m (4 ft) on center, respectively. The results showed that the revised code equation (TMS 2013) could still be unsafe as the spacing of the vertical grouted cells and the amount of horizontal reinforcement increases. Bolhassani et al[6,7] tested planar PGM walls with aspect ratios of 0.6 and 1.0, and vertical grouted cells spaced at 1.8 m (6 ft). They examined walls with single, separately grouted, reinforced cells, as commonly done in practice, and walls with double, side-by-side, grouted cells and joint reinforcement as an improved alternative. Their results showed that the shear capacity predicted by the revised equation in TMS 2013 was up to 1.8 times higher than the experimental value. The revised equation, however, accurately predicted the capacity of a PGM wall assemblage tested by Johnson and Schultz[8] that had a window opening, wall flanges, and the same spacing of vertical grouted cells as the walls of Bolhassani et al.[6,7] Maleki[9] tested PGM walls that had various aspect ratios and spacings of grouted cells. He reported that the shear-strength predictions of both the Canadian Masonry Standard[10] and US code (MSJC 2008) were acceptable.

Earlier studies in New Zealand on nominally reinforced PGM walls were summarized by Ingham et al.[11] Voon and Ingham[12] tested two planar PGM walls that had no bond beams and were not subjected to any applied axial load. The two wall specimens had vertical grouted cells spaced at 0.4 m (1.3 ft) and 0.8 m (2.6 ft) on center, respectively. It can be shown that the revised shear strength formula in TMS 402 (2013) underestimates the strength of the wall that had more closely spaced grouted cells by 20%, but it provides a good estimation of the strength of the wall that had the larger spacing. In a different experimental study, Voon and Ingham[13] investigated the influence of different configurations of openings in PGM walls that were not subjected to any applied axial load and had vertical grouted cells spaced at 0.8 m (2.6 ft) on center. The walls developed severe stair-stepped cracks along mortar joints in the ungrouted panels but exhibited gradual strength and stiffness degradation. It was shown that the wall strength decreased as the height of the wall opening increased.

The behavior of PGM wall systems, designed according to current standards in the United States, under real earthquake excitation has not been well studied. Shake-table tests conducted on fully grouted masonry wall systems have revealed that a wall system can behave very differently than what was assumed in the design. For example, unintended coupling forces exerted by horizontal diaphragms on shear walls may alter the behavior of a wall from the intended ductile flexural mode to a brittle shear mode (Stavridis et al[14]). In addition to the coupling effect, axial restraints exerted by walls orthogonal to the direction of the seismic action can also change the axial forces in the walls parallel to the seismic force and thereby their resistance mechanism (Mavros et al[15]).

This paper presents the results and findings from the shake-table tests of a full-scale, one-story, PGM structure designed according to the current code provisions. A nonlinear finite element model has been developed and validated with the test results and has been used to understand the load resistance mechanism of the structure, the distribution of the shear resistance among the wall components, and the influence of bond beams on the seismic performance. The numerical results have also been used to evaluate the shear-strength equation of the current code.

2 | PROTOTYPE BUILDING AND SPECIMEN DESIGN

2.1 | Prototype building configuration

Figure 1 shows the hypothetical one-story prototype building considered in the experimental study. The structure was assigned Seismic Design Category (SDC) C, which is defined in ASCE/SEI 7 (2010), representing a structure located in a moderate seismic zone in the central or eastern United States. The structural system consists of gravity frames in the outer area and RM walls in the central part. The RM walls are arranged in four modules, each designed to carry seismic as well as gravity loads. As in typical design, the gravity frame is not intended to resist earthquake forces. The roof consists of 152 mm (6 in.) thick precast hollow-core planks with a 51-mm (2 in) cast-in-place RC topping. Each masonry wall module carries a tributary gravity load of 338 kN (76 kips) from the roof and has a tributary seismic weight (W) of 1784 kN (401 kips), which includes the weight of 1/4 of the entire roof and the self-weight of the masonry walls above the level of the window sills. The walls are partially grouted and their design conforms to the requirements for ordinary load-bearing RM shear walls, which have the seismic force modification factor $R = 2$, according to ASCE/SEI 7 (2010) and TMS 402 (2013), reflecting limited ductility that is acceptable for SDC C. The design spectral intensity considered is $S_{DS} = 0.5$ g, which is the upper end for SDC C. Hence, the resulting design base shear for each wall module is $V_b = 446$ kN (100 kips).

The wall and diaphragm configurations selected for the hypothetical prototype building were to achieve a minimum code-compliant wall system that would barely meet the seismic demand specified for SDC C, so that the safety of the existing design code for PGM could be accessed. It should be noted that in many situations, single-story RM buildings have more walls than needed to resist design seismic forces. Additional walls are often included for architectural functions, such as building envelopes or interior partitions. Nonetheless, minimum code-compliant situations could arise in multistory buildings where the bottom-story walls could be subjected to high seismic forces transmitted from the upper stories. However, such type of structures would be too costly to test in this study; therefore, a single-story prototype building that had less walls than typical buildings was considered. Another deviation from typical construction is that single-story buildings often have flexible light-weight roof diaphragms. The performance of these buildings would be dominated by the in-plane deformation of the roof diaphragms and the out-of-plane response of the masonry walls. Because the focus of this study was on the in-plane seismic response of PGM walls, a stiff roof diaphragm was selected, which would also provide the additional weight to reach to the amount of seismic force needed.

2.2 | Design of test structure

As shown in Figure 1, the test structure represented one of the four masonry wall modules. It was symmetric about the center lines in the east-west and north-south directions and had a door and a window opening in each of the south and north walls. The structure was tested on a shake table with the table motion applied in the east-west direction only. As shown in Figures 1 and 2, the wall components separated by openings are labeled as W1, W2, and W3 on the south

FIGURE 1 Hypothetical prototype building and reinforced masonry test structure [Colour figure can be viewed at wileyonlinelibrary.com]
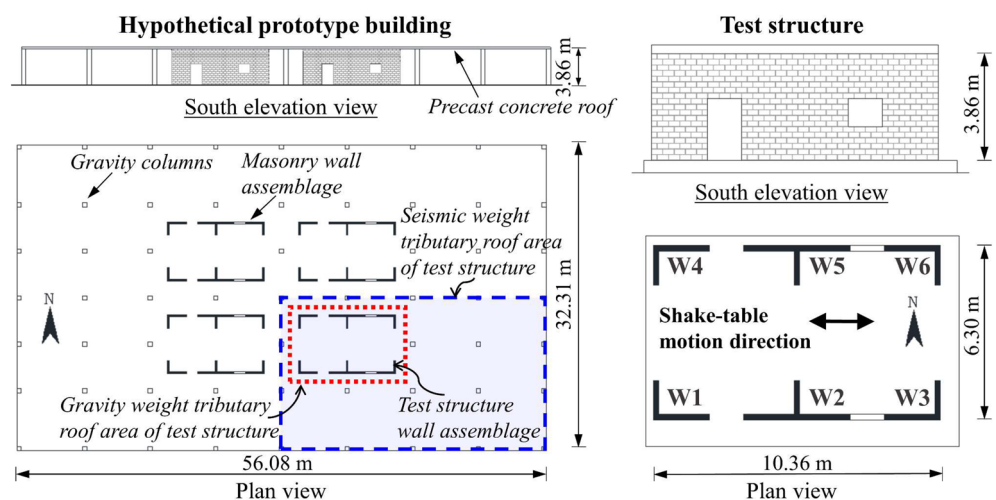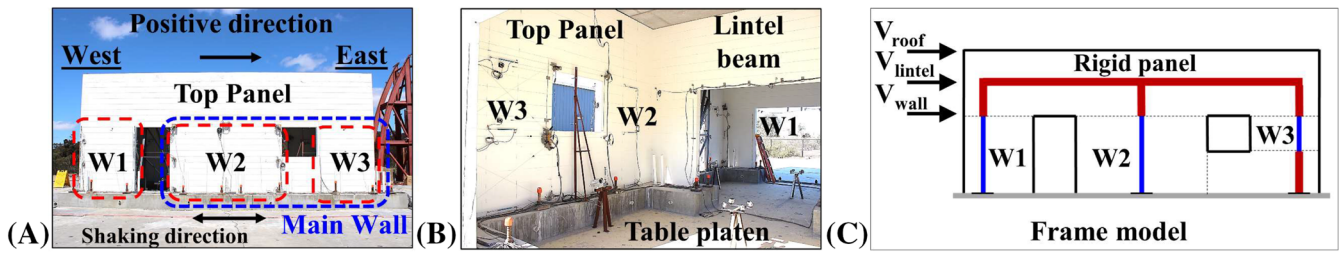
FIGURE 2 Shake-table test specimen and frame model used for design. (A) South view of specimen; (B) south-east view of interior of specimen; (C) plane frame model [Colour figure can be viewed at wileyonlinelibrary.com]

side, and W4, W5, and W6 on the north side. Each of the corner walls, W1, W3, W4, and W6, had an L-shaped cross section, and each of the middle walls, W2 and W5, had a T-shaped cross section. Lintels spanned along the north-south direction between W1 and W4, W2 and W5, and W3 and W6. The whole panel consisting of W2 and W3 (or W5 and W6) including the window up to the elevation of the top of the window opening is referred to as the main wall, and the masonry panel above the openings is identified as the top panel. The masonry walls had a height of 3.86 m (152 in.) and a nominal thickness of 203 mm (8 in.).

For ordinary walls, shear-capacity design is not required by TMS 402. For the given wall configuration, one or more of the wall components were expected to be dominated by shear. A shear-dominated wall with light horizontal reinforcement may lose its lateral load resistance quickly after reaching the peak shear strength. Hence, it was prudent to assume in the design that the base shear capacity of the structure would be reached when the shear demand on any of the shear-dominated wall components reached its shear strength. The design was assisted with an elastic analysis based on this premise. The resulting reinforcement details for the test structure are illustrated in Figure 3. The vertical and horizontal reinforcement consisted of Grade 60 #4 (129 mm^2) bars. The reinforcement met the prescriptive requirements of the code in that the area of the vertical reinforcement adjacent to the openings and wall intersections was at least 129 mm^2 (0.2 in.^{2}), and the vertical and horizontal bar spacing did not exceed 3.0 m (120 in.). The building had four bond beams along the height. One was in the first course above the footing, the second and third were right below and above the window opening, and the fourth was in the upper-most course right below the roof. The bond beam in the top course was required to accommodate dowel bars to tie the roof diaphragm to the masonry walls. The bond beam at the bottom course was introduced to provide a better performance (e.g., to reduce base crushing) if the walls were to develop base sliding. Although the code requires that bond beams be placed right below and above a window or door opening, they need not be extended continuously along the entire wall length unless they are required to resist shear. For this structure, the two intermediate bond beams were not required by the design to resist shear, but they were deemed beneficial for resisting the strut action that could be developed by the ungrouted masonry panels.
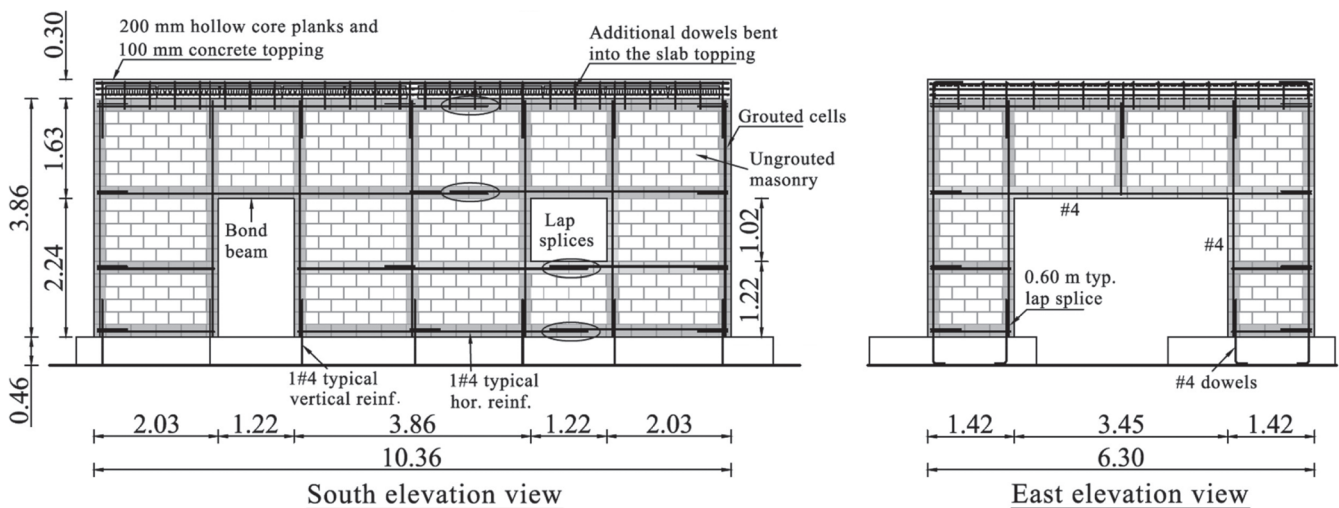
FIGURE 3 Reinforcement details for the test specimen (the dimensions shown are in meters)

The roof system consisted of 203-mm-thick (8 in.) precast hollow-core planks with a 102-mm (4 in.) cast-in-place RC topping. It was much thicker than that of the prototype to attain the targeted roof weight of 338 kN (76 kips) without the need to include the tributary roof area outside the wall module. The seismic weight of the test structure was 535 kN (120 kips). That included the weight of the roof and that of the masonry walls above the level of the window sills.

2.3 | Supporting analysis

The reinforcement details were verified via elastic analysis. Because of the structure's symmetry, only the wall on one side (south or north) was considered. A linearly elastic plane-frame model, as shown in Figure 2C, was employed to calculate the seismic force demand on wall components W1, W2, and W3. Timoshenko beam elements were used to represent the wall components, whereas the top panel and the portion of W3 below the window sill were assumed to be rigid. For W1 and W2, the reinforcement in the two lower bond beams would contribute to the shear strength, whereas no bond beam would be present in W3 based on the wall height assumed. The net cross-sectional areas of the walls were considered. For calculating the flexural strengths of the walls, the entire flange width was considered effective, which complied with the code specification for flange in tension (TMS 402). The equivalent lateral load was distributed in the way shown in Figure 2C, with V_{roof} proportional to the weight of one-half of the roof slab and applied at the level of the roof, V_{lintel} proportional to the weight of the top panel and half of the transverse lintels and applied at the midheight of the top panel, and V_{wall} proportional to the weight of the walls between the top panel and the window sill and applied at the top of the door opening. This was based on the assumption that the roof and the top panel displaced as a rigid body. Forces V_{lintel} and V_{wall} only account for 8.3% and 2.7% of the total base shear demand.

The lateral seismic forces were applied in the positive and negative directions. The compressive strength of masonry was specified to be 12.6 MPa (1.83 ksi) based on the net area of the walls. Table 1 shows the seismic load demands on W1, W2, and W3 when the lateral load applied to the entire test structure is equal to the design base shear of 446 kN (100 kips), the capacities of the wall components calculated according to the code-specified methods, and the capacity-to-demand ratios. It can be seen that all wall components were shear-dominated apart from W1, which was flexure-dominated when subjected to positive loading. Furthermore, W3 had a capacity-to-demand ratio slightly greater than 1.0, whereas the other two wall components had much higher ratios. Hence, W3 controlled the design.

3 | CONSTRUCTION, MATERIAL PROPERTIES, AND INSTRUMENTATION

The walls of the test structure were constructed on RC footings that were post-tensioned onto the shake-table platen. Figure 4 shows pictures of the construction. The top surface of the footings was not intentionally roughened. The walls were constructed by professional masons following standard masonry construction practices. The whole construction took 12 days to complete. Standard $203 \times 203 \times 406$ mm ($8 \times 8 \times 16$ in.) CMUs were used for the ungrouted part of the walls, double open-end units (H-blocks) were used for the bond beams, and open-end and half open-end units were used at the locations having vertical grouted cells. For both the head and bed joints, mortar was applied only at the face shell of the blocks. The units were laid in a running bond pattern with interlocking at the intersections of the orthogonal walls at the four corners of the structure (see Figure 4B). However, the orthogonal walls in the middle of the

TABLE 1 Load demand and capacity of the wall components with the design base shear applied in the positive (pointing east) and negative direction

Wall	Axial Load, P_u (kN)		Lateral Load Demand, V_u (kN)		Flexural Capacity, V_{flex} (kN)		Shear Capacity, V_n (kN)		Min $(V_{flex}, V_n)/$ V_u	
	Neg.	Pos.	Neg.	Pos.	Neg.	Pos.	Neg.	Pos.	Neg.	Pos.
W1	137.1	32.4	40.1	40.2	209.1	157.0	163.3	165.7	4.08	3.91
W2	111.3	81.1	83.1	83.5	485.4	441.7	293.2	291.3	3.53	3.49
W3	19.2	154.1	99.8	99.3	330.6	478.1	115.1	137.0	1.15	1.38

Note: Strength factors of 0.9 and 0.8 were used in the calculation of the flexural and shear capacities, respectively, according to TMS 402. Axial loads with positive sign represent compression.
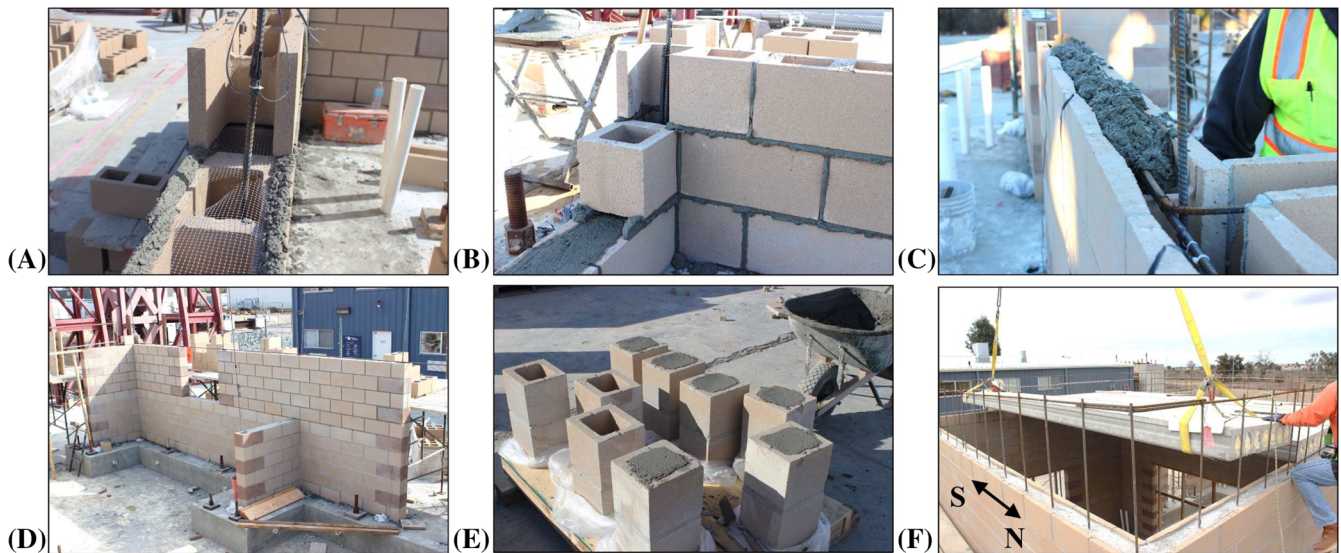
FIGURE 4 Construction of the structure on the shake table. (A) Second bond beam; (B) a corner wall; (C) grouting of the second bond beam in a T-wall; (D) south main wall; (E) grouted and ungrouted masonry prisms; (F) placement of roof planks [Colour figure can be viewed at wileyonlinelibrary.com]

structure were simply connected through the reinforcing bars in the bond beams without interlocking units (see Figure 4C,D). The horizontal bars in the bond beams extended from the web into the flange with 90° bents, whereas standard 180° hooks were used at the wall ends. During construction, every bond beam course was grouted together with the vertical reinforced cells below. A net was placed under each bond-beam course (see Figure 4A) to prevent the grout from flowing into the cavity below. The grout was consolidated appropriately by means of mechanical vibration. Observations during and after the tests indicated that the grout had been placed properly. The vertical bars were lap-spliced above the footings over a length of 0.6 m (24 in.), which was more than the minimum length specified in the code, whereas the horizontal bars were lap-spliced at the locations shown in Figure 3. The precast roof planks spanned along the north-south direction and were simply supported on the south and north walls (see Figure 4F). After the placement of the planks, the vertical dowel bars from the walls were bent 90°. After the placement of reinforcement in the north-south and east-west directions on the planks, the concrete topping was poured.

Coarse grout with 9.5-mm (3/8 in.) aggregate and Type S mortar were used for the construction of the masonry walls. Material samples were taken during the construction and were tested during the period of the shake-table testing at an age exceeding 28 days. Compression tests were conducted on 51 × 102 mm (2 × 4 in.) mortar cylinders, 95 × 95 × 193 mm (3.75 × 3.75 × 7.625 in.) grout prisms prepared per ASTM C1019, grout cylinders, two-unit tall grouted and ungrouted masonry prisms per ASTM C1314, single CMU blocks, and concrete cylinders sampled from the footing concrete and the roof topping. All masonry prisms were prepared with half CMU blocks as shown in Figure 4E. The average compressive strength obtained for each sample type is summarized in Table 2. Furthermore, tension tests were conducted on samples of the reinforcing bars used in the masonry walls. The average yield strength obtained was 481 MPa (70 ksi), and the average tensile strength was 690 MPa (100 ksi) and was attained at a strain of 0.113.

The shake-table test structure was instrumented with an array of 393 sensors, consisting of 177 strain gages, 177 displacement transducers, and 39 accelerometers. The strain gages were attached on the vertical and horizontal reinforcing bars at locations where yielding could occur. Linear potentiometers were used to measure sliding along bed joints and uplift of the walls at certain locations. They were also mounted vertically at the two sides of W1 and W4 to determine

TABLE 2 Average compressive strengths obtained from material samples

Sample	Strength	Sample	Strength	Sample	Strength	Sample	Strength
Mortar cylinders	27.6 MPa	Grout prisms	41.9 MPa	Ungrouted masonry prisms	14.0 MPa	Concrete footings	43.6 MPa
Grout cylinders	29.0 MPa	Grouted masonry prisms	18.2 MPa	CMU	21.7 MPa	Concrete roof topping	32.5 MPa

the curvature along the height of these walls. Sliding at the base of the structure was also monitored with linear potentiometers installed along the base of the walls. The horizontal displacement of the roof with respect to the base of the walls was measured at the top of the north and south walls with two string potentiometers (one per side). The potentiometers were installed at the top bond-beam course and the strings were attached to steel reference frames, which were 3.75 m (148 in.) tall and mounted on the concrete footings. The acceleration at the base and the roof was measured with accelerometers placed on top of the footings and the roof slab, respectively. The complete instrumentation plan can be found in Koutras and Shing.[16] In addition to the conventional sensors, the deformations of the walls on the north and west sides of the structure were monitored with a digital image correlation (DIC) system using high-speed cameras. However, the system was only employed for a limited number of tests before any major structural damage occurred. Further details are presented in Rajaram et al.[17]

4 | GROUND MOTIONS AND SCALING

The test structure was subjected to a sequence of 17 earthquake motions, referred to as motions 1 to 17, which were historical records that were scaled to different intensity levels. In most of the tests, the north-south component of the El Centro record from the 1940 Imperial Valley Earthquake (EC1940) was used. A record from the 1979 Imperial Valley Earthquake was used for motions 2 and 3, and two records from the 2011 Mineral, Virginia Earthquake and the 1985 Nahanni Earthquake were used for motions 1, 7, and 10. Nonetheless, the motions using the last three records did not induce any discernible damage to the structure and therefore are omitted from the following discussion.

The estimated seismic weight of the test structure was $W_{spec} = 535$ kN (120 kips), whereas the seismic weight considered in the design of the wall module based on the prototype configuration was $W = 1784$ kN (401 kips). The difference is due to the tributary weight carried by the gravity columns, which was not included in the test structure. For the test structure to satisfy the dynamic similitude with the prototype, the applied base acceleration in the tests was scaled up by a factor of $F_a = W/W_{spec} = 3.33$, and the time was compressed by a factor of $F_t = (1/F_a)^{0.5} = 0.55$. This scaling was applied to the ground motion records for tuning the shake table prior to the construction of the specimen. The actual seismic weight of the test structure as constructed was calculated to be 559 kN (126 kips), which was only slightly higher than the initial estimation. Before motion 1 and after each earthquake motion, the structure was subjected to white-noise excitation with a root-mean-square amplitude of 0.05 g to identify any change in the natural period. The initial fundamental period ($T_{initial}$) of the test structure was identified to be 0.043 s. This initial period, according to the similitude scaling, corresponds to a period of 0.078 s for the prototype structure. Given the geometry of the masonry walls, this value seems reasonable, and it is consistent with what was observed in full-scale RM structural systems previously tested on a shake table that had floor and roof diaphragms similar to the one used in this study.[14,15]

Figure 5 shows the time history of motion 17 and compares the response spectra of motions 8 and 17, which were obtained by the accelerometers placed on the footings of the test structure, to the spectra for the Maximum Considered Earthquake (MCE) and the Design Earthquake (DE), which were also scaled according to the similitude law. The MCE is 1.5 times the DE. The shake table was tuned with ground motions scaled to the DE with the procedure described in Luco et al.[18] However, as shown in Figure 5B, when the intensity of the motions increased, the table did not track the input motion closely, and the response spectra of the table motions showed a significant amplification in the frequency range of 10–20 Hz, where the resonance frequency of the oil column of the shake table resided. To quantify the
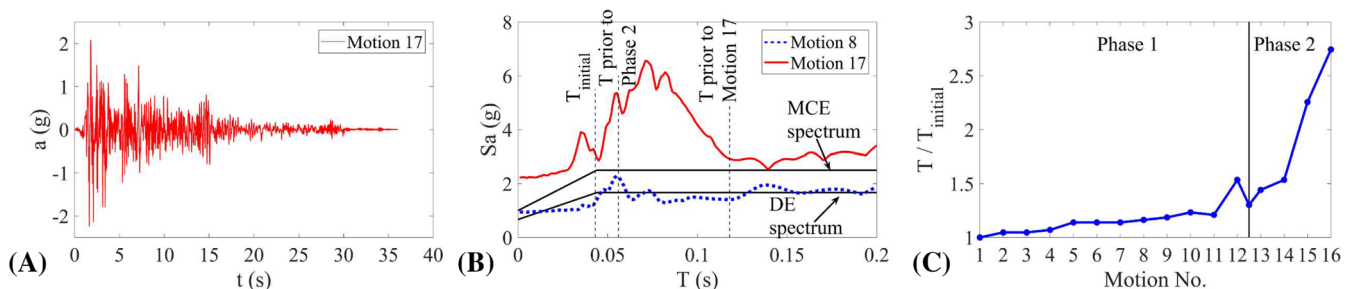
FIGURE 5 Ground motions and structural period change. (A) Acceleration time history of motion 17; (B) acceleration response spectra of motions 8 and 17; (C) structural period measured after each test [Colour figure can be viewed at wileyonlinelibrary.com]
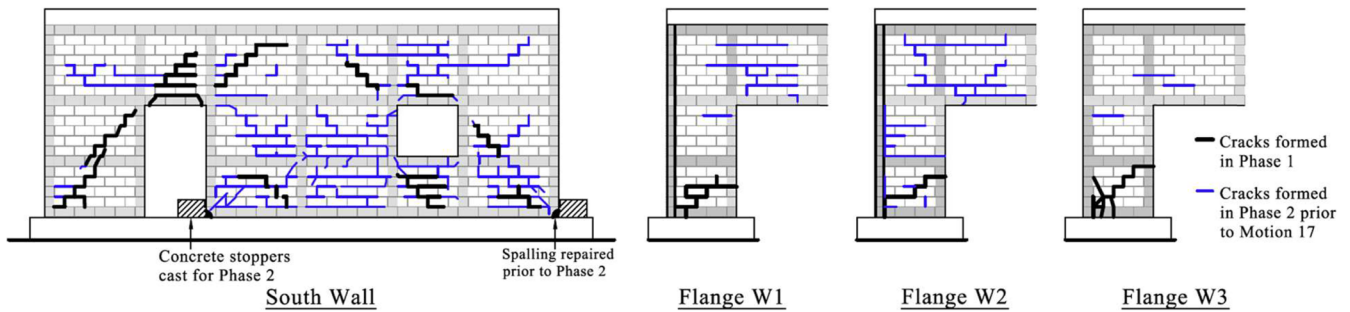
FIGURE 6 Cracks formed in the south wall and flanges in phases 1 and 2 up to motion 16 [Colour figure can be viewed at wileyonlinelibrary.com]

intensity of the table motions in a meaningful manner, the ratio of the spectral acceleration of the motion to the one of the MCE is used as an effective intensity measure (I_{eff}). The ratio is calculated as the average value over the range of the structural period measured before and after the application of the ground motion (Stavridis et al[19]).

5 | STRUCTURAL BEHAVIOR AND ANALYSIS OF TEST DATA

Testing was conducted in two phases. In phase 1, the structure was tested in its original configuration. After a number of tests and before the walls reached their flexural or shear capacities, the response started to be dominated by the sliding of the main walls at the base. To restrain sliding in the subsequent tests, RC blocks (stoppers) were cast against the bottom course of the main walls on both sides, as can be seen in Figures 7 and 8. The subsequent tests are referred to as phase 2. Some minor damage induced in phase 1 near the toes of the main walls was repaired with grout patch. Rubber pads were placed between the concrete stoppers and the wall toes to allow for a uniform distribution of the contact forces. Before the first phase-2 test, the fundamental period of the structure was measured to be 0.056 s, which was only slightly longer than the fundamental period of 0.043 s measured at the beginning of phase 1 indicating that the masonry walls had not sustained major damage.

Table 3 shows the sequence of the major tests conducted in phase 1 and all the tests in phase 2, for which the EC1940 record was used, and summarizes peak response quantities along with the effective intensity of the motions and the value of the structural period measured after each test. It should be noted that the peak response quantities shown for each motion are not necessarily concurrent. For the calculation of the net roof drift ratio shown in the table and subsequent figures, the sliding measured at the base of the main walls was subtracted from the roof displacement. The net roof drift was divided by the clear height of the roof, which was 3.86 m (152 in.), to obtain the drift ratio. The base shear shown in the table is calculated considering the mass of the structure above the window sills, which is
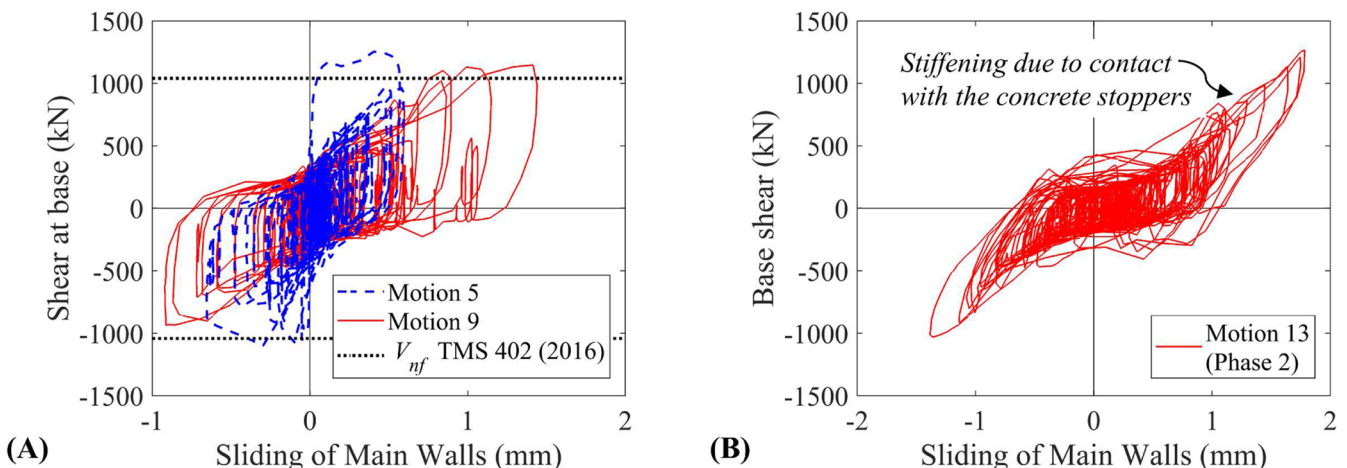
FIGURE 7 (A) Shear force at base versus base sliding response during motions 5 and 9; (B) base shear versus base sliding response during motion 13 [Colour figure can be viewed at wileyonlinelibrary.com]

FIGURE 8 Damage obtained before, during, and after motion 17 in the test and analysis (time instants of max. drift, point 1 and point 2 are marked in Figures 9 and 15) [Colour figure can be viewed at wileyonlinelibrary.com]

consistent with how the design base shear was determined. The change of the structural period during phases 1 and 2 is shown in Figure 5C. The decrease of the structural period at the beginning of phase 2 was mainly due to the repairs at the toes of the main walls.

5.1 | Response in phase 1

In phase 1, the structure was subjected to 12 motions, which had the effective intensity I_{eff} ranging from 0.36 to 1.91. The structure developed sliding at the base when the effective intensity of the applied motion reached the MCE level (i.e., when I_{eff} was around 1.0). In the first 11 motions, no discernible damage was observed in the masonry walls, yet the sliding measured at the base of the main walls was consistently larger than that of W1 and W4. During motion 12, which was the most demanding motion in phase 1 with $I_{eff} = 1.91$, the sliding at the base of the main walls increased reaching 6.2 mm (0.24 in.), which was almost equal to the peak roof displacement, as shown in Table 3. The sliding at the base of W1 and W4 was much smaller and diagonal cracks formed in their webs. No significant damage was observed in the main walls apart from some fine cracks along mortar joints and the spalling of the grouted cells at

TABLE 3 Summary of structural response during the tests

Motion No.	Test ID[a] (EC1940 Record)	Testing Phase	Specimen Period After Test, s	Eff. Intensity I_{eff}, x MCE	PGA, g	Peak Roof Accel., g	Peak Roof Disp., mm	Peak Base Sliding, mm W1/W4	Main walls	Peak Net Roof Drift Ratio[b], %	Peak Base Shear, kN
4	125%-A	Phase 1	0.046	0.81	−1.36	−1.37	−0.7	0.0	0.0	−0.02	767
5	188%-A		0.049	1.05	−1.91	−1.96	1.4	0.2	−0.7	0.02	1095
6	84%-A		0.049	1.15	0.94	−1.73	2.0	0.3	0.8	0.03	970
8	84%-B		0.050	0.69	0.95	−1.30	1.6	0.3	0.7	0.04	706
9	125%-B		0.051	1.23	1.33	−1.79	2.9	0.8	1.4	0.04	1002
11	125%-C		0.052	1.46	1.29	−1.79	4.1	1.3	2.2	0.05	1004
12	164%-A		0.066	1.91	−1.73	−1.94	−7.1	−1.5	−6.2	0.06	1087
13	125%-D	Phase 2	0.062	1.52	−1.49	−1.98	4.2	2.1	1.8	0.06	1105
14	164%-B		0.066	2.04	−1.88	−2.16	5.7	2.6	1.8	0.10	1210
15	188%-B		0.097	2.07	−2.09	−2.22	6.7	3.4	−1.9	0.13	1240
16	202%		0.118	1.43	−2.16	−2.27	−8.9	4.1	−1.9	−0.18	1269
17	214%		n.a.	1.17	−2.24	−2.21	87.4	7.1	−1.8	2.25	1236

[a]Test ID indicates the scaling of the original EC1940 record on top of the similitude scaling. The letter A, B, C, or D next to the percentage indicates the 1st, 2nd, 3rd, or 4th time the same motion was applied. Motions 4 and 5 had the positive and negative directions flipped as compared to the other records.

[b]The net roof drift ratio is the roof displacement subtracted by the sliding measured at the base of the main walls and then divided by the clear height of the roof.
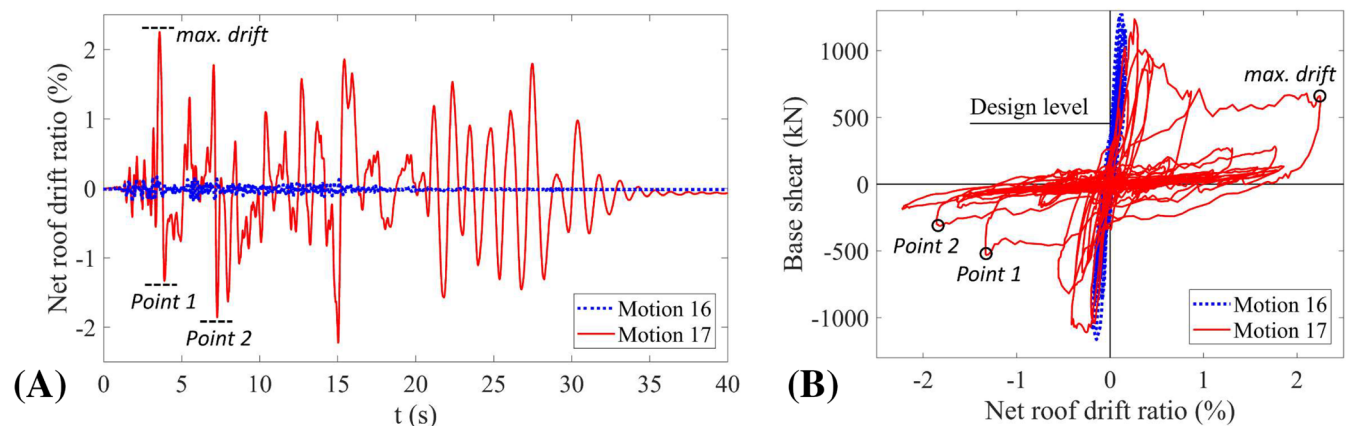
FIGURE 9 Structural response during motions 16 and 17. (A) Net roof drift ratio time-history response; (B) base shear versus net roof drift ratio hysteresis curves [Colour figure can be viewed at wileyonlinelibrary.com]

the wall toes caused by the sliding. Almost identical sliding displacements were obtained at the three transducer locations along the base of each main wall. Sliding was not observed in the wall flanges. Instead, fine stair-stepped cracks developed along mortar joints near the base of the flanges. Figure 6 shows the cracks formed on the south wall and flanges during phase 1. Data from the vertical displacement transducers placed along the wall-foundation interface of the slender wall components, W1/W4, indicate that there was partial uplift along the wall base. However, even when that occurred, part of the wall base was still in contact with the foundation slab providing shear transfer.

Figure 7A shows the total shear force at the base plotted against the base sliding registered at the main walls during motions 5 and 9. Both motions did not cause any visible cracking in any of the masonry walls, and motion 5 was the motion during which base sliding initiated. The shear force in the figure is the total lateral force transmitted to the base of the structure and is calculated as the sum of the inertial force of the roof slab and the total inertial force of the walls. The figure shows a large shear force developed in the positive direction during an early cycle in motion 5. This shear-

friction resistance can be largely attributed to the clamping force exerted by the vertical reinforcement. However, as the grout surrounding the dowels at the base got damaged, the bond between the dowels and the grout deteriorated leading to a reduction of the clamping force and thereby a drop in the shear-friction resistance at the same displacement levels in the subsequent cycles. The small increase in the shear resistance as sliding increased could be attributed to the restoring forces developed by W1 and W4 and the wall flanges, as well as the dowel action.

According to TMS 402 (2016), the shear-friction strength (V_{nf}) for walls with a low aspect ratio is given by $V_{nf} = \mu (A_{sp}f_y + P_u)$, where μ is the coefficient of friction, P_u is the axial load, and $A_{sp}f_y$ (the total area of vertical reinforcement crossing the sliding plane, excluding that in the wall flanges, times the yield strength) represents the clamping force of the vertical reinforcement crossing the sliding plane. Applying this formula here, only the 14 #4 vertical bars in the in-plane walls needs to be considered. With the assumption that the coefficient of friction μ is 0.7, as recommended in TMS 402 (2016) for masonry walls laid on concrete surface that was not intentionally roughened, the formula results in a sliding resistance of 1041 kN (234 kips), which is very close to the maximum sliding resistance developed during motion 5, as shown in Figure 7A. However, it should be noted that the wall flanges and dowel action could also contribute a small portion of the shear resistance once sliding had started. It should also be noted that not every vertical reinforcement crossing the sliding plane yielded during motion 5. The strains in the vertical reinforcement measured 2.5 cm (1 in.) above the footing surface were in the range of 30%–100% of the yield strain.

5.2 | Response in phase 2

In phase 2, the structure was subjected to five motions with effective intensity above the MCE (see Table 3). With the stoppers installed, the peak sliding at the base of the main walls was limited to 2 mm and was due to the deformation of the rubber pads that had been placed between the stoppers and the wall toes. Figure 7B shows the base shear versus base sliding response during motion 13. It can be observed that the base shear resistance started to increase after a certain amount of sliding occurred, when the rubber pads got compressed. At the base shear capacity of the structure, which was reached during motion 16, the peak base sliding in the main walls constituted 24% of the total roof displacement. However, at the maximum roof drift, which was reached in motion 17, the last run, the peak base sliding of the main walls was only 1% of the total roof displacement. The structure withstood motions 14 and 15, which had effective intensities more than two times the MCE, without showing signs of major damage. Instead, fine cracks developed mainly along mortar joints of the main walls in a stair-stepped pattern and diffused minor cracking occurred in masonry units. Similar level of damage was observed in motion 16 with the peak net roof drift ratio reaching only 0.18%. Figures 6 and 8A show the state of the structure after motion 16 and the corresponding crack pattern.

The photos in Figure 8B–F depict the damage states of the structure during and after motion 17. Figure 8 also shows the corresponding damage states obtained from a finite element analysis, which will be discussed later. During motion 17, the existing cracks propagated through the vertical grouted cells causing rapid load degradation. A maximum net roof drift ratio of 2.25% was reached and was accompanied by severe cracking of the vertical grouted cells, and cracking and crushing of ungrouted units, as shown in Figure 8B. It appears that among the wall components, W3/W6 were the first ones to develop the most severe damage and the other walls followed. By the end of motion 17, severe damage had occurred in the grouted cells, and most of the ungrouted units within the height of the window openings in the main walls and below the mid-height of W1/W4 were damaged and dislocated from the walls, leaving large openings, as
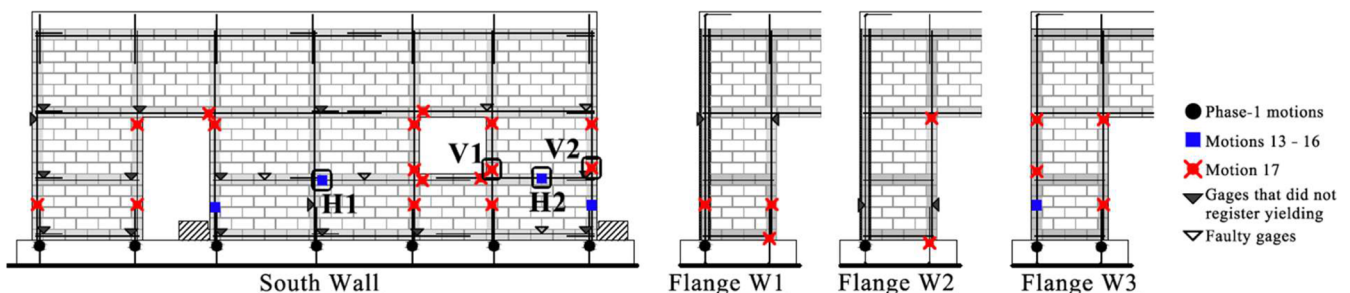
FIGURE 10 Yielding of reinforcement at the locations of the strain gages of the south wall and flanges [Colour figure can be viewed at wileyonlinelibrary.com]

shown in Figure 8E/F. The wall flanges experienced heavy damage as well; yet, they were able to carry the weight of the roof after the end of the test averting total collapse of the building. The state of damage of the test structure at points 1 and 2, after the attainment of the peak roof drift before the end of motion 17, as identified in the response-history plot in Figure 9, is shown in Figure 8C,D.

Figure 9 shows the time histories of the net roof drift ratio and the hysteresis curves obtained during motions 16 and 17. The maximum base shear developed in the positive direction was 1269 kN (285 kips), which occurred in motion 16 at a net roof drift of 0.13%. In the negative direction, the maximum base shear reached was 1131 kN (254 kips). During motion 17, severe load degradation occurred within the first few cycles before the structure reached a net roof drift of 0.4%. The damage resulted in a significant reduction of the lateral stiffness which led to large displacement oscillations even under very low base acceleration towards the end of the input motion (see Figure 5A), as shown by the net drift history after the first 20 s. At the time of the maximum net roof drift of 2.25%, the drift ratio experienced by the main walls was 4% because most of the wall deformation concentrated below the top panel. This drift level is much higher than that reached in any of the previous experimental studies on PGM walls; yet the test structure was still able to retain a significant residual lateral strength, which was almost equal to 50% of the peak base shear. However, the resistance dropped significantly upon displacement reversal and in the subsequent cycles due to the loss of masonry from the walls.

5.3 | Yielding of reinforcement

The sequence of yielding in the reinforcing bars as recorded by the strain gages is illustrated in Figure 10. Only the south wall and the connected flanges are shown because a similar yielding sequence was observed in the walls on the north side. The motion during which each strain gage registered yielding for the first time is indicated. The gages that did not record yielding as well as the faulty ones are also indicated. For brevity, the sequence of yielding during the different motions in phase 1, as well as during motions 13 through 16, is not identified. During the phase-1 tests, the vertical bars yielded along the base of the wall due to tension induced by base sliding. In phase 2, most of the additional yielding occurred during motion 17. However, the yielding of the reinforcement in the second bond beam (from the base) of W2 and W3 was first observed in motion 16, during which the maximum base shear was reached.

Figure 11 shows the strains plotted against the net roof drift obtained during motions 16 and 17 in the second bond beam of W2 and W3 at the locations H1 and H2 marked in Figure 10. During motion 16, the strains barely exceeded the yield strain. Furthermore, the plots show that the reinforcement in the second bond beam of W3 was engaged primarily during drift in the positive direction (towards east). This could be because for positive drifts, diagonal shear cracks intercepted the bond beam, whereas for negative drifts, the shear cracks were localized within the panel next to the window. For the same reason, the bond beam of W2 was engaged when the drift was towards the negative direction. During motion 17, the strain in the reinforcement of the bond beam of W3 increased rapidly until the net roof drift reached 0.5% in the positive direction. Beyond that drift, the deformation of W3 localized in the masonry panel next to the window, which is consistent with the damage shown in Figure 8C–F. Figure 11 also shows the strains developed in the two vertical bars in W6 at locations V1 and V2 indicated for W3 in Figure 10. The bars developed significant strains after the net roof drift reached 1%, which was in the post-peak regime of the base shear versus net roof drift curves.
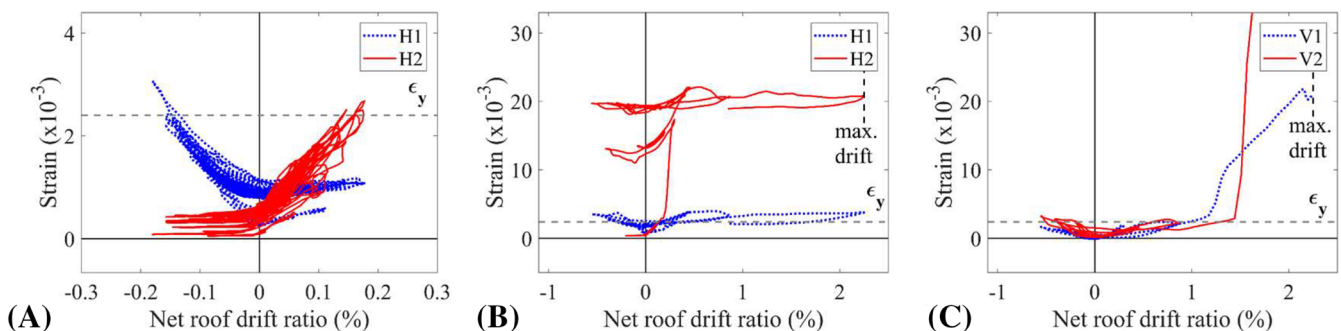
FIGURE 11 Strains from selected strain gages plotted against the net roof drift ratio. (A,B) Strains recorded by gages H1 and H2 during motion 16, and during motion 17, respectively; (C) strains recorded during motion 17 in the vertical bars of W6 at the respective locations V1 and V2 [Colour figure can be viewed at wileyonlinelibrary.com]
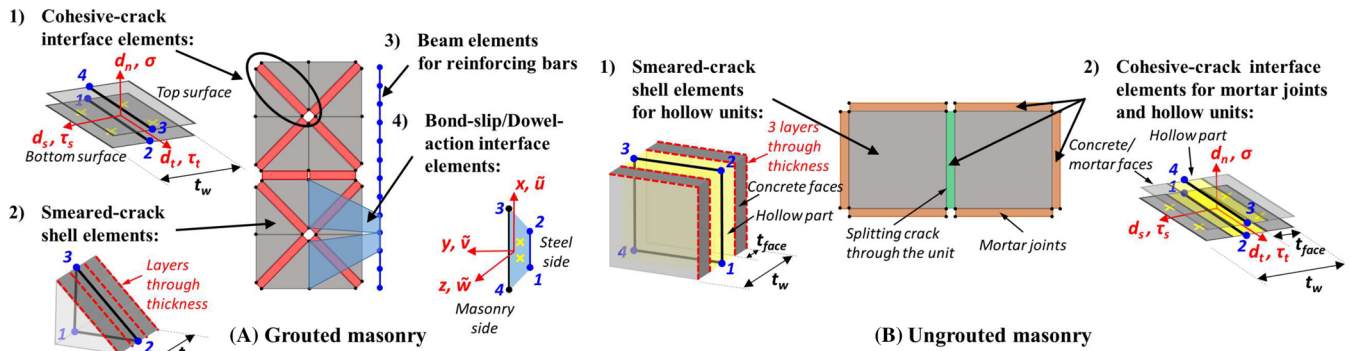
FIGURE 12 Finite element modeling scheme for grouted and ungrouted masonry [Colour figure can be viewed at wileyonlinelibrary.com]

6 | FINITE ELEMENT MODELING

The maximum base shear developed in the tests was 2.8 times the design base shear. The fact that the actual material strengths in the test structure were higher than the nominal strengths, and the strength reduction factors introduced in the design (see Table 1) can only explain part of this overstrength. The main contributing factor is the conservative design assumption that the capacity of the structure was limited by the capacity of walls W3/W6, whereas W1/W4 and W2/W5 had reserve capacities, as shown in Table 1. To acquire a better understanding of the lateral load resisting mechanism of the structural system, a detailed finite element (FE) model has been developed for the test structure. The model is used to examine the lateral resistance developed in each wall component, which is hard to deduce from the test data. The modeling scheme and numerical results are presented in the following sections.

6.1 | Modeling scheme

As shown in Figure 12, four types of elements are used to model a PGM wall. Smeared-crack shell elements and cohesive-crack interface elements are used to simulate the behavior of masonry. Beam elements are employed to model the reinforcing bars in a discrete manner. Additional interface elements are used to connect the beam elements to the adjacent masonry shell elements to simulate the bond-slip and dowel-action behaviors of the reinforcing bars. The FE program LS-DYNA[20] has been used as the platform, in which the required material models, and the cohesive-crack and bond-slip/dowel-action interface elements have been implemented as user-defined features.

The grouted masonry is modeled with triangular smeared-crack shell elements to simulate the compressive behavior of masonry as well as diffuse cracking. Each triangular element has two perpendicular sides that are 102-mm (4 in.)
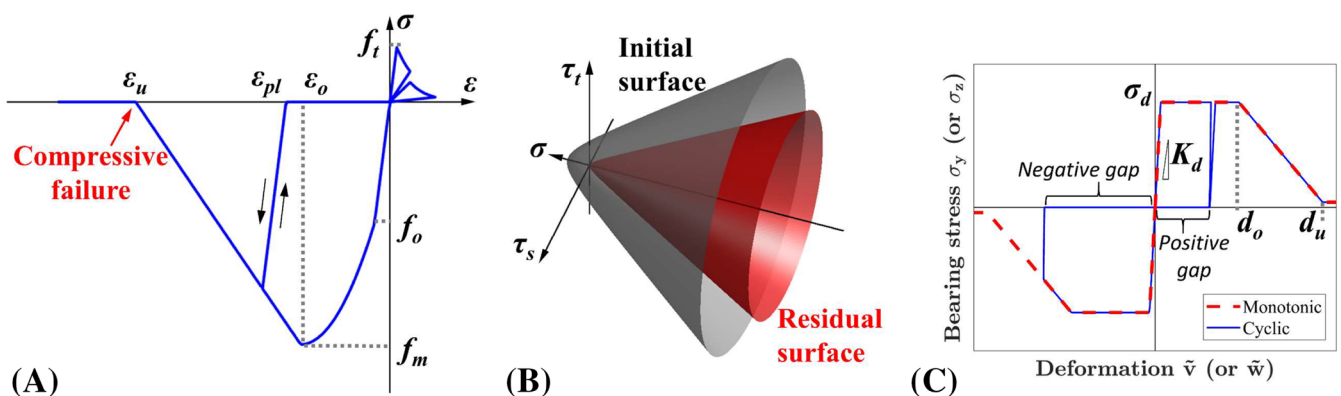
FIGURE 13 Material models. (A) Uniaxial stress-strain law for the orthotropic model for masonry; (B) initial and residual failure surfaces for the cohesive-crack law; (C) dowel-action model [Colour figure can be viewed at wileyonlinelibrary.com]

long. Cohesive-crack interface elements are used to represent dominant cracks in a discrete fashion. They are placed at a 45° angle to capture diagonal shear cracks in a realistic manner, avoiding stress locking that could be introduced by smeared-crack elements (Rots and Blaauwendraad[21]; Lotfi and Shing[22]), and in the horizontal direction to allow for an accurate simulation of sliding along a cracked joint. For the ungrouted masonry, each CMU is represented by two 203 × 203-mm (8 in.) quadrilateral smeared-crack shell elements with a vertical cohesive-crack interface element placed in-between to simulate possible splitting cracks through the unit. Only the thickness of the face shells of the CMU is considered for the ungrouted masonry. The thickness of each face shell is 35.6 mm (1.40 in.). Cohesive-crack interface elements are also used to represent the horizontal and vertical mortar joints.

6.2 | Element formulations and constitutive models

Shell elements with transverse shear deformation (LSTC[20]) are used to model the walls. To simulate the out-of-plane bending of the walls, each shell element is assigned three material layers through the thickness. For the triangular elements representing grouted masonry, the three layers have equal thickness with uniform material properties. A single Gauss point is assigned to each layer. For the quadrilateral shell elements representing ungrouted masonry, the two exterior layers represent the face shells of the masonry units, whereas the interior layer represents the void and has a dummy material with zero resistance. Each layer of the quadrilateral elements has four integration points.

The smeared-crack model used with the shell elements adopts a simple and robust orthotropic material law. Before cracking, the axes of orthotropy are aligned and rotate with the directions of the principal strains. Cracking initiates when the maximum principal stress reaches the specified tensile strength of the material. Beyond that point, the axes of orthotropy remain fixed, with directions parallel and perpendicular to the direction of the first crack. Another crack can develop in the direction perpendicular to the first crack when the tensile stress parallel to the first crack exceeds the tensile strength. The uniaxial stress-strain law for tension and compression in each of the orthotropic directions is shown in Figure 13A. Interaction in compression between the two orthotropic directions is modeled in a simplistic manner by assuming that the residual plastic strain ε_{pl} in compression is the same for both directions and has a magnitude equal to the larger of the two developed in these directions. The material is assumed to have failed (with the strength dropping to zero) when the compressive strain exceeds ε_u.

Discrete cracks and mortar joints are modeled with zero-thickness interface elements which allow differential crack opening and sliding. Similarly to the shell elements, the interface elements used for the ungrouted masonry account for the void as shown in Figure 12B. The stress state is expressed in terms of one normal and two shear stresses and is determined with a cohesive-crack plasticity model which was developed by Koutromanos and Shing[23] and Kottari.[24] The model can simulate mixed-mode fracture, crack opening and closing, and shear sliding. Failure is determined by the yield surface shown in Figure 13B the evolution of the which is governed by a set of softening rules to simulate the strength degradation due to the gradual loss of cohesion and the decrease of the friction coefficient. Under cyclic shear deformation, the model accounts for the reversible joint dilatation caused by the wedging effect of the interface asperities and can also simulate irreversible joint compaction due to the loss of the damaged material. This is particularly important for simulating the response of shear-dominated PGM walls since the dilatation or compaction of the mortar joints will affect the stresses transmitted from the surrounding grouted masonry.

The steel reinforcing bars are modeled with beam elements that have the formulation by Hughes and Liu.[20] The beam elements used in this study have a single integration section along the length and a total of four fibers for the integration of stresses over the cross section. The stress-strain response of each fiber is described by the uniaxial steel model of Kim and Koutromanos.[25] The material model accounts for bar fracture due to low-cyclic fatigue. A beam element representing a reinforcing bar is considered to be fractured when all the fibers of the section have fractured. Fracture of a fiber is triggered when a scalar damage parameter, which is based on the cumulative plastic work of the tensile stress, exceeds a specified critical value. The failure criterion is based on the recommendation of Moharrami and Koutromanos.[26]

The interface elements that are used to simulate the bond-slip and dowel action have three deformation components: the relative shear displacement $\tilde{u}$ between the bar and masonry along the axial direction of the bar, and the relative displacements $\tilde{v}$ and $\tilde{w}$ normal to the slip, which represent the deformation of masonry adjacent to the bar and the opening and closing of the gap created by dowel action along the two directions. The bond stress due to slip is modeled by the cyclic bond-slip law proposed by Murcia-Delso and Shing.[27] The bearing stresses introduced by dowel action are calculated with the simple uniaxial material law shown in Figure 13C, with the initial stiffness and yield stress

FIGURE 14 Front and back view of the FE model of the test structure [Colour figure can be viewed at wileyonlinelibrary.com]
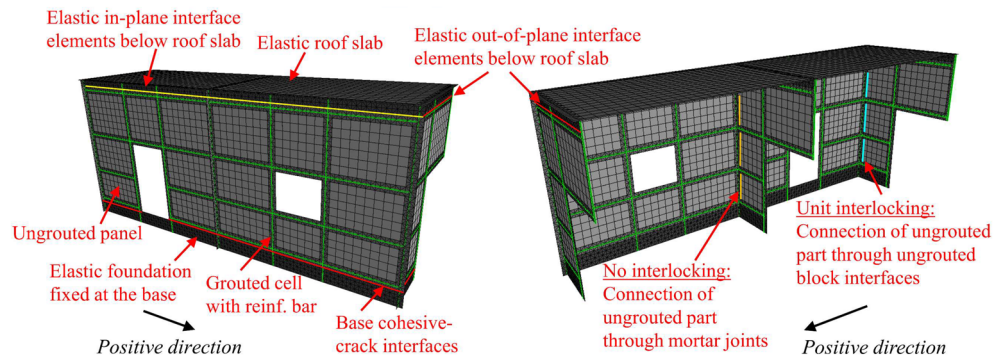
determined with the dowel model proposed by Dulacska[28] and the linear softening branch calibrated from quasi-static wall test data. The response along each of the dowel directions is assumed to be independent of the other. For calculating the dowel strength, the compressive strength of the grout is used, whereas for determining the bond strength, the average of the compressive strengths of the grout and the masonry prism is used. The interface element has been implemented based on the formulation proposed by Mavros[29] and Kottari et al.[30]

6.3 | Element removal scheme

An element removal scheme has been implemented to accurately model severe masonry crushing and reinforcement fracture and to simulate the loss of contact between masonry units under certain conditions. In the analyses, element removal is triggered by the following set of rules. When all the integration points in a shell element satisfy the condition for compressive failure, the shell element, all the adjacent cohesive-crack interface elements, and all the connected bond-slip/dowel-action interface elements are removed. When all the integration points of a beam element have registered fracture, the beam element and the adjacent bond-slip/dowel-action interface element are removed. A cohesive-crack interface element is removed when one of the integration points registers out-of-plane sliding that is larger than the thickness of the wall for the grouted masonry, or larger than the thickness of the face shell for the ungrouted masonry. In addition, the interface element representing a mortar bed joint is removed when its lower nodes drop by an average of 51 mm (2 in.) with respect to the top. Finally, any shell element that is attached only on one side to another element will be removed. For ungrouted masonry, a shell element will be removed even if it remains connected through two of its sides but the interface representing the bed joint below has already been removed.

6.4 | Analysis of the test structure

The FE modeling scheme presented above has been used for the dynamic and pushover analysis of the test structure. As shown in Figure 14, only the south half of the structure is modeled, with appropriate boundary conditions applied to the nodes at the plane of symmetry. The vertical interface elements between the grouted and ungrouted masonry assume the properties of ungrouted masonry units, which are perceived to constitute the plane of weakness. The footings and the roof slab are modeled with elastic shell elements. The walls are connected to the footings through cohesive-crack interface elements, whereas stiff elastic interface elements are used to connect the walls to the roof slab. The lap-splices at the bottom of the walls are modeled explicitly. The 180° hooks and the 90° bends of the horizontal bars around the vertical bars are considered in an approximate manner by directly attaching the node of the horizontal bar to the node of the vertical bar. The weights of the roof slab and the masonry are distributed over the respective areas. Because the roof planks were initially supported only by the in-plane walls (see Figure 4F), the interface elements placed between the slab and the out-of-plane walls are activated after the vertical loads have been applied.

The material models adopted have a number of parameters to specify. The cohesive-crack interfaces simulating the fracture of grouted masonry and CMU blocks are assigned a high initial stiffness. The initial modulus of elasticity for the smeared-crack model representing the grouted masonry is specified to be $600f'_m$, which is less than $900f'_m$ recommended by TMS 402. This is based on the prism test data of Mavros.[29] For the ungrouted units, it is assumed to be $600f_b$, where the f_b is the compressive strength of the units. The elastic normal stiffness of the mortar interfaces is
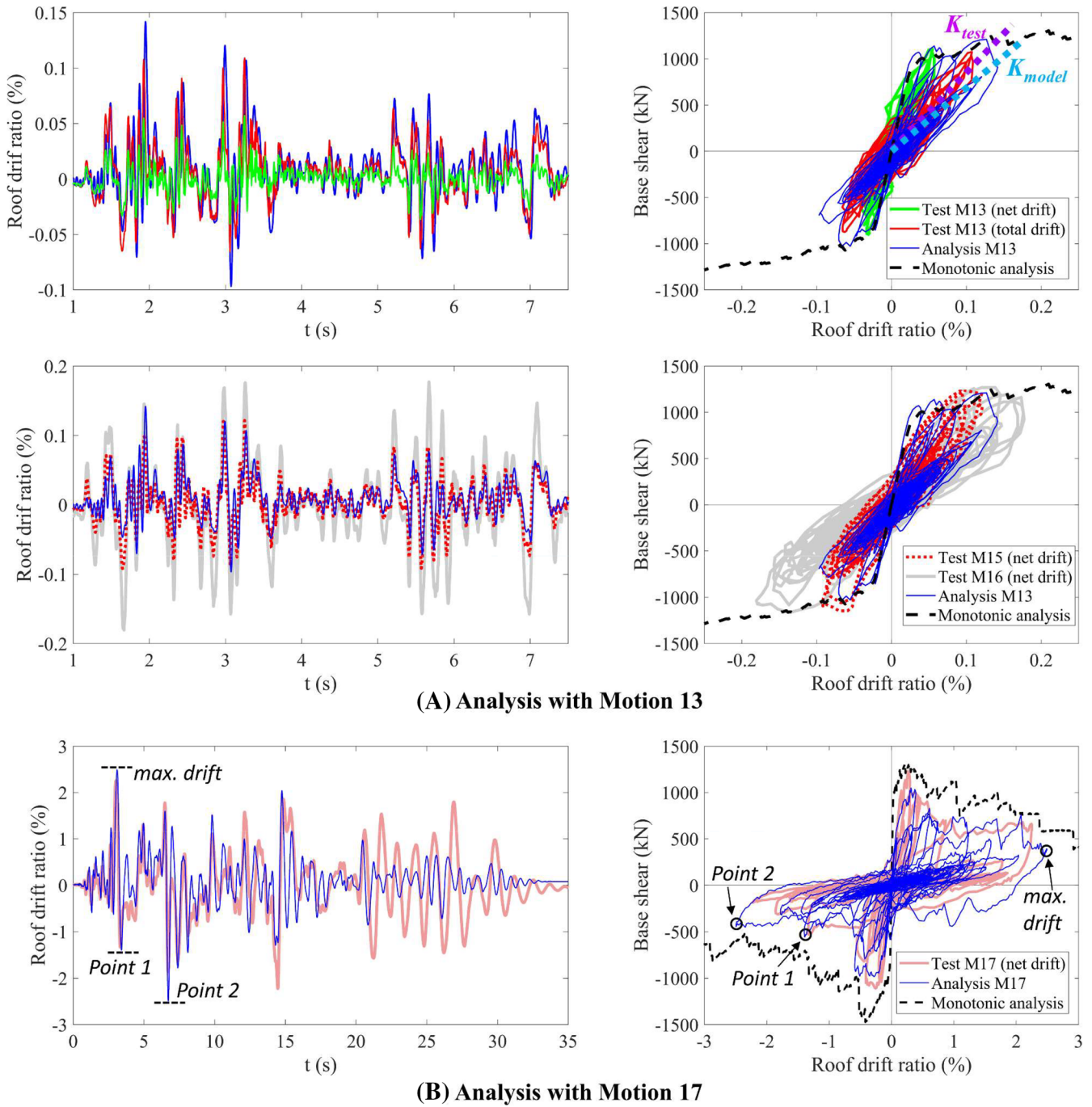
FIGURE 15 Comparison of numerical and experimental results [Colour figure can be viewed at wileyonlinelibrary.com]

calibrated so that the stiffness of the ungrouted masonry prism is $600f'_m$. The compressive strengths of the grouted and ungrouted masonry are determined from the prism tests and the yield and tensile strengths of the reinforcement from the tension tests. The tensile strength for the grouted masonry is taken to be 12% of the average of the compressive strength of the grout (41.9 MPa) and that of the grouted masonry prisms (18.2 MPa). The tensile strength of the CMU is assumed to be 12% of f_b. Other material parameters, such as the compressive and tensile fracture energies of masonry, the tensile strength of mortar joints, and the other parameters defining the cohesion, friction, dilatation, and compaction of the cohesive-crack model are based on the recommendations from the literature.[23,31,32]

The time-history analysis is performed with the implicit time-integration scheme proposed by Bathe.[33] The scheme has a desirable numerical damping characteristic to suppress spurious high-frequency modes that could be induced by the cracking of masonry. Additionally, Rayleigh damping is prescribed with a damping ratio of 0.1% for the first and

second modes. Its stiffness proportional part is based on the initial stiffness of the shell and beam elements. However, for the cohesive-crack and bond-slip/dowel-action interface elements, no stiffness proportional damping is applied because of their high initial stiffness. The initial fundamental period of the model is calculated to be 0.044 s. However, it should be noted that the mass of the model is 6% higher than that of the test structure because of the meshing scheme.

Ground motion histories measured at the base of the structure during the shake-table tests are used for the time-history analysis. Because the structure did not sustain any major damage during phase 1, only the phase-2 tests are considered. Instead of explicitly modeling the concrete stoppers, the surface of the footings is assumed to be sufficiently rough to prevent base sliding. To this end, a coefficient of friction of 1.0 is used in the model. The structure is subjected to motions 13 and 17 in a single run. Motions 14 through 16 are not considered because the damage observed in the analysis with motion 13 is slightly more severe than that obtained with motion 15 in the test. Figure 15 compares the net roof drift time histories and the hysteresis curves obtained from the analysis and the test. For Figure 15A, only the response for the first 7.5 s of motion 13 is shown for clarity. The lateral resistance is calculated by summing the shear forces developed in the horizontal interface elements at the top of the second bond beam course (the level of the window sill) and the shear forces developed by the dowel action of the vertical reinforcement at the same elevation. This is consistent with the method used to calculate the seismic force from the experimental data by considering only the seismic mass above that line. The damage patterns obtained in the analysis before and after the application of motion 17 as well as at the time instants of the maximum roof drift and the peak drift points after that, which are marked in the response-history plot of Figure 15B, can be found in Figure 8.
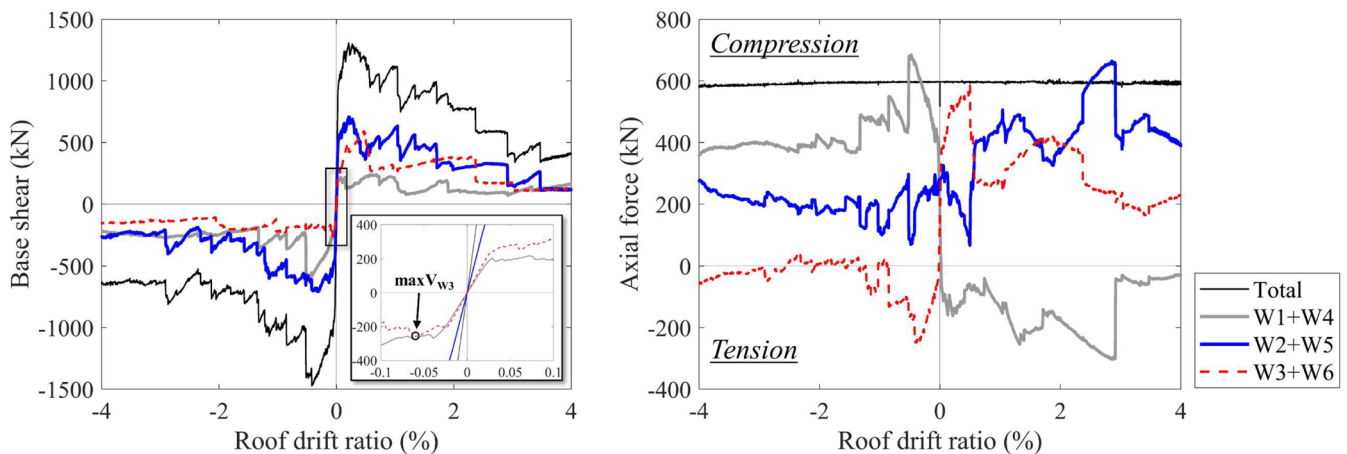
FIGURE 16 Shear and axial force developed by each wall component in the pushover analysis [Colour figure can be viewed at wileyonlinelibrary.com]
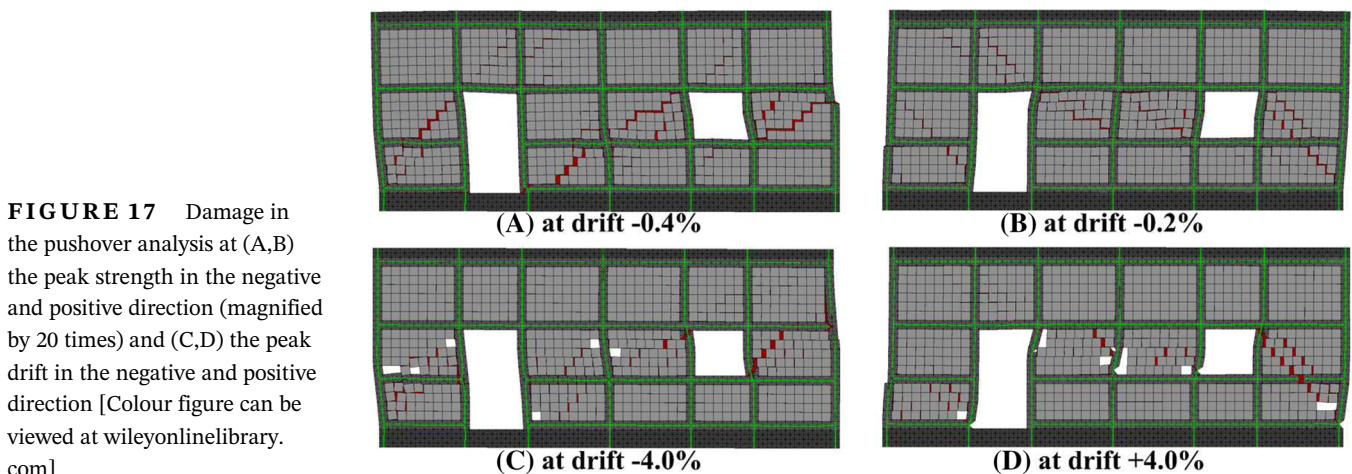
FIGURE 17 Damage in the pushover analysis at (A,B) the peak strength in the negative and positive direction (magnified by 20 times) and (C,D) the peak drift in the negative and positive direction [Colour figure can be viewed at wileyonlinelibrary.com]

(A) at drift -0.4%

(B) at drift -0.2%

(C) at drift -4.0%

(D) at drift +4.0%

In Figure 15A, the experimental results with motion 13 are presented is terms of both the net and the total roof drift ratios. The latter includes the base sliding. It can be seen that the base sliding developed under motion 13 constitutes almost 50% of the peak roof displacement (see also Table 3). In the analysis, the deformation mechanism is different because the base sliding of the model is practically zero. The walls in the model develop a larger amount of deformation and damage compared with that of the specimen under the same motion. The fact that the total roof drift history in the test is not too different from the roof drift in the analysis is likely because the two cases eventually exhibit a similar secant stiffness, as can be deduced from the base shear versus total roof drift curves of Figure 15A. The secant stiffness shown for each case on the plot corresponds to the peak total roof drift. The difference with respect to the structural (effective) period that can be derived from the secant stiffness of each case is smaller. In the test, although the concrete stoppers were engaged (see Figure 7B), the peak base shear developed was lower than the base shear capacity of the walls. However, in the analysis, the base shear capacity of the walls is attained. The two lower graphs in Figure 15A show that the peak lateral drift obtained in the analysis with motion 13 is in-between the values obtained for motions 15 and 16 in the tests but closer to the test response for motion 15. For motion 17, the model captures the response in the first 10 s of the motion (see Figure 15B) and is also able to reproduce the rapid loss of resistance observed in the test. However, for the rest of the motion, it overestimates the stiffness and thereby the response frequency of the structure. This could be attributed to the less severe damage induced in the vertical grouted cells and wall flanges of the model as compared with the actual test structure (see Figure 8E,F). Nonetheless, the analysis captures the extent of damage in the ungrouted panels of the in-plane walls reasonably well. Furthermore, the crushing and removal of the shell elements occurred primarily after reaching the maximum positive roof drift (see Figure 8B) as in the test.

6.5 | Distribution of forces among wall components

To gain insight into the distribution of the seismic force among the wall components and also the lateral load capacity of each wall component, a pushover analysis is performed with the FE model. The displacement is applied at the level of the roof, in the positive and negative directions. Figure 16 compares the shear and axial forces developed in each wall component at the level of the window sill. The total lateral resistance and vertical load of the structure are also shown. The axial force in each wall is calculated by summing the normal forces in the horizontal interface elements of the in-plane and out-of-plane walls and the forces of the vertical bars. It can be observed that the pushover analysis shows a more gradual load degradation and a higher peak resistance than the time-history analysis (as compared in Figure 15). However, for the positive direction, the difference in the strength is small (with 1306 vs. 1211 kN).

The numerical results show that W1/W4 and W3/W6 develop a higher strength in the loading direction that induces axial compression, whereas W2/W5, the middle wall component, shows a very small difference in the two loading directions, for which the axial load is always compressive but varies in magnitude. Figure 17 shows the deformed meshes obtained for each loading direction. It can be seen that the diagonal cracks in W2 spread along the height of the window for positive loading, but those associated with negative loading spread over the height of the door opening. Wall component W3 behaves in the opposite way. The analysis shows that the horizontal reinforcement in the second bond beam of W3 is engaged only when the building is subjected to positive loading. This behavior is consistent with what was observed from the test data (see Figure 11A). Yielding in the reinforcement of the bond beam occurs before the structure develops its maximum load capacity. The reinforcement eventually fractures at a roof drift ratio of 2.5%.

To evaluate the code provisions, the shear and flexural strengths of each wall component are calculated with the methods recommended in TMS 402 using the axial force (P_{Vmax}) developed in the pushover analysis at the peak lateral resistance of each wall component. The wall components are assumed to have fixed-fixed end conditions. Based on the

TABLE 4 Calculation of lateral load strengths of the wall components based on TMS 402

Wall	V_{max} (kN) Analysis Neg.	Pos.	P_{Vmax} (kN) Analysis Neg.	Pos.	Shear Span Ratio (M/Vd) Neg.	Pos.	Effective Hor. Reinf. Neg.	Pos.	V_{flex} (kN) TMS 402 Neg.	Pos.	V_n (kN) TMS 402 Neg.	Pos.	Min (V_{flex}, V_n) /V_{max} Neg.	Pos.
W1	301.5	115.8	342.0	−46.4	0.55	0.55	2 #4	2 #4	457.3	125.0	226.3	170.0	0.75	1.08
W2	352.4	359.7	116.1	119.7	0.29	0.13	2 #4	None	608.8	1352.3	339.5	315.1	0.96	0.88
W3	129.0	297.0	−41.0	294.2	0.25	0.55	None	2 #4	285.2	417.7	147.4	226.3	1.14	0.76

FIGURE 18 Response of different designs subjected to the 1940 El Centro scaled by a factor of 1.6 [Colour figure can be viewed at wileyonlinelibrary.com]

(A) Original design   (B) Intermediate design   (C) Minimum reinf. design
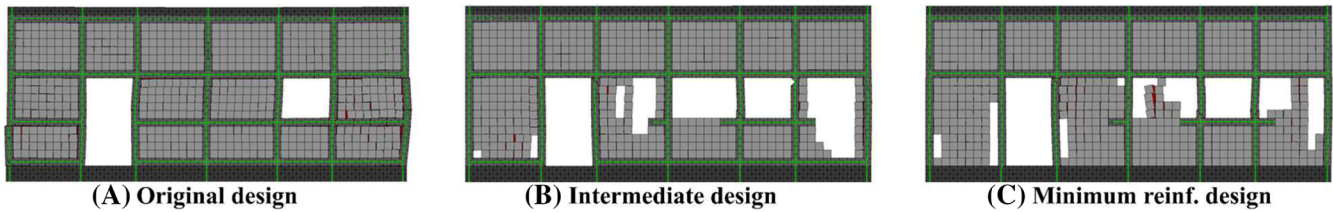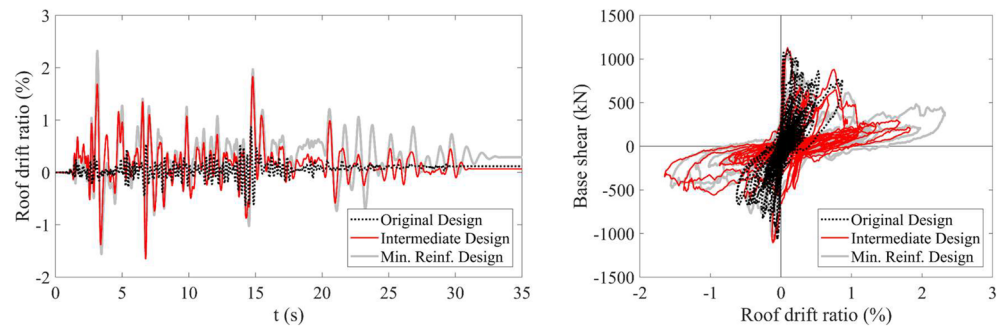
FIGURE 19 Damage induced by the 1940 El Centro record scaled by a factor of 1.6 [Colour figure can be viewed at wileyonlinelibrary.com]

observations from the pushover analysis and the tests, different heights are assumed for each of W2 and W3 depending on the direction of loading. For positive loading, W2 is assigned the height of the window and W3 the height of the door. For negative loading, W2 is assigned the height of the door and W3 the height of the window. The height of W1 is assumed to be the same as the door opening. The masonry prism strengths and the yield strength of the steel reinforcement obtained from the material tests are used. The shear strength is calculated based on the ungrouted masonry prism strength, whereas the flexural strength is based on both the ungrouted and grouted masonry prism strengths depending on the wall cross-sectional area under compression.

Table 4 shows the code-based shear strength (V_n) and flexural strength (V_{flex}) as compared with the wall strengths obtained from the pushover analysis. Based on the code-based capacities, W2 and W3 are shear dominated for both loading directions, whereas W1 is shear dominated for negative loading and flexure dominated for positive loading. The shear-strength equation of TMS 402 overestimates the capacity of W3 by 14% when the building is subjected to negative loading and W3 is under tension. For the rest of the shear-dominated cases, the code equation gives a lower value. The difference between the code value and the numerical result is higher for W1 under negative loading and for W3 under positive loading. This could be due to the beneficial influence of the wall flange, which enhances the shear-compression resistance at the wall toe. Furthermore, assuming that W3 has the height of the door opening when the building is subjected to positive loading is also a conservative hypothesis. For W1 loaded in the positive direction, the code-based flexural capacity is slightly higher than the analysis result. This can be explained by the mixed flexural-shear mode W1 developed in the pushover analysis and also by the fact that the top of W1 is not perfectly fixed.

The results obtained from the pushover analysis reveal that the distribution of the shear resistance among W1, W2, and W3 is different from the one assumed in the design, which was based on an elastic analysis (see Table 1). The design assumed that the capacity of the system was reached once the shear capacity of one wall component was reached. Based on this premise, the design was governed by the shear capacity of W3 for both loading directions. For the negative loading direction, the pushover analysis shows that W3 indeed reaches its load capacity before W1 and W2 because it is subjected to tension; however, the capacity of W3 is relatively small and is still able to maintain a portion of its resistance as the displacement increases. The capacity of the structure is reached when both W1 and W2 almost reach their capacities as shown in Figure 16. At that point, the two wall components together provide 87% of the lateral load resistance of the structure. For loading in the positive direction, the analysis shows that the maximum load resistance of the structure develops when W2 reaches its peak strength. In this case, W2 together with W3 provide 90% of the maximum total load resistance. Wall component W1 that is in tension reaches its maximum load after W2 and W3

have lost their peak strengths. For either loading direction, the wall component in tension provides only a small portion of the lateral resistance. However, it contributes to a higher axial compression in the other two wall components, and therefore, indirectly enhances the shear resistance of the structure.

6.6 | Influence of bond beams

As previously discussed, the wall components would still meet the design load demand, and the prescriptive requirements of TMS 402 even if the first and second bond beams (from the base), except for the portion of the bond beam right under the window openings, were not present. To evaluate the influence of the bond beams on the performance of the structure, two code-compliant design alternatives are considered. The first alternative has the bond beam under the window openings extend only 0.6 m (24 in.) beyond the left and right sides of the openings rather than through the entire length of the main walls. Furthermore, the second bond beam in W1/W4 is removed. The second bond beam is also removed from all the wall flanges except for the middle flange, which requires a bond beam to connect to the main wall because the wall joint has no interlocking masonry units. This design is referred to as the intermediate design. The second alternative is the same as the first but has all the bond beams at the base course removed as well. This is referred to as the minimum reinforcement design.

To compare the two alternative designs with the original design of the test structure, time-history analyses are performed with the FE models representing the three designs using the original 1940 El Centro record scaled by a factor of 1.6. This motion corresponds to a spectral intensity of 1.22 times the MCE at the fundamental period of the model. The ground motion is scaled to comply with the dynamic similitude with the prototype building. Similar to the previous analyses, the interface between the wall and the footing is assumed to be rough. Figure 18 compares the response time histories and load-displacement hysteresis curves. The damage induced for each case is shown in Figure 19. One can see that the second bond beam can significantly improve the performance of the structure. It provides a horizontal tie to effectively confine the ungrouted masonry. The influence of the bond beam at the base is not as significant, but it is still beneficial in that it slightly reduces the drift level. However, the Intermediate Design, which includes the base bond beam, has more crushing in the ungrouted masonry, resulting in a more extensive element removal than the minimum reinforcement design. Base sliding is not observed in any case.

7 | CONCLUSIONS

This paper presents an experimental and numerical study on the seismic performance of a single-story partially grouted reinforced masonry structure. The structure was designed according to the current code provisions in the United States for areas of moderate seismicity. The design of the masonry walls was based on an elastic frame model and the assumption that the capacity of the wall system would be reached when one of the shear-critical wall components first reached its shear capacity. The structure was tested on a shake table with a sequence of ground motions. Under the first MCE-level motion, the structure developed a response dominated by base sliding. The sliding resistance calculated with the shear-friction equation in TMS 402 (2016) using a coefficient of friction of 0.7 closely matches the shear-friction resistance deduced from the test data. In the second phase of testing, base sliding was restrained with RC stoppers, and the test structure developed its ultimate base shear capacity showing fine cracks along the mortar joints and some limited yielding of the reinforcement in the bond beams. The base shear capacity reached was 2.8 times the design base shear. In phase 2, the structure was able to withstand four motions with an effective intensity above the MCE level before failing in a brittle manner. Two of the motions had an effective intensity of two times the MCE. The structure exhibited a significant load degradation at a roof drift of about 0.4%. However, it was able to maintain almost 50% of its lateral load capacity at a roof drift of 2.25%, which corresponds to an actual drift ratio of 4% for the main walls.

The behavior of the structure has been further studied with nonlinear FE analyses. The FE model gives a reasonable prediction of the response time histories and the strength of the structure, as well as the load degradation observed in the tests. A pushover analysis has been conducted to investigate the contribution of the wall components to the lateral load capacity of the structural system. The analysis has shown that the elastic frame model used in the design did not give the correct load distribution among the wall components. Furthermore, it has shown that even the shear-dominated wall components are able to retain a substantial portion of their load capacities at displacements beyond the point of their peak lateral resistance. This allowed different wall components of the structure to develop significant

lateral resistance at the same time, and for the resistance to further increase as the axial compressive loads in the walls increase, resulting in a base shear capacity much higher than the design base shear (2.8 times). The numerical results have also been used to assess the shear-strength equation of TMS 402 (2013, 2016). It has been found that the shear strength of the wall components calculated with the code equation is slightly lower than those given by the FE model, except for wall components W3/W6 when subjected to tension. The results have also indicated that the wall flange may improve the shear resistance when it is in compression. Furthermore, the FE analyses have shown that the continuous bond beams right below the window openings appear to significantly improve the performance of the structure. The benefit of a bond beam in the first course above the footing is negligible if sliding does not occur.

Even though conservative, the assumptions used to design the structure appear to be adequate considering the brittle behavior exhibited in the test after the roof drift exceeded 0.4%. The overstrength factor of 2.8 is close to the value of 2.5 suggested by ASCE/SEI 7 for ordinary load-bearing RM shear walls. Further investigation is needed to understand why the shear-strength equation in TMS 402 significantly overestimates the shear capacities of wall components tested in some other studies. In particular, the influence of the spacing of grouted cells, the wall aspect ratio and boundary conditions, and the applied loading history should be investigated.

ORCID

Andreas A. Koutras https://orcid.org/0000-0002-9556-3812

REFERENCES

1. TMS 402. *Building Code Requirements for Masonry Structures*. Longmont, CO: The Masonry Society; 2013, 2016.
2. ASCE. *Minimum Design Loads for Buildings and Other Structures*. Reston, VA: ASCE/SEI 7; 2010, 2016.
3. Clough RW, Gülkan P, Manos GC. Seismic testing of single-story masonry houses: part 2. *J Struct Eng*. 1990;116(1):257-274.
4. Minaie E, Mota M, Moon FL, Hamid AA. In-plane behavior of partially grouted reinforced concrete masonry shear walls. *J Struct Eng*. 2010;136(9):1089-1097.
5. Nolph SM, ElGawady MA. Static cyclic response of partially grouted masonry shear walls. *J Struct Eng*. 2012;138(7):864-879.
6. Bolhassani M, Hamid AA, Johnson C, Moon FL, Schultz AE. New design detail to enhance the seismic performance of ordinary reinforced partially grouted masonry structures. *J Struct Eng*. 2016;142(12):1–15, 04016142.
7. Bolhassani M, Hamid AA, Moon FL. Enhancement of lateral in-plane capacity of partially grouted concrete masonry walls. *Eng Struct*. 2016;108:59-76.
8. Johnson CA, Schultz AE. *Simulated Seismic Testing of Partially-Grouted Masonry Sub-Assemblages*. Anchorage, Alaska: Proc. 10th U.S. National Conference on Earthquake Engineering; 2014.
9. Maleki M. Behaviour of partially grouted reinforced masonry shear walls under cyclic reversed loading. PhD dissertation, McMaster University, Hamilton, Ontario, Canada, 2008.
10. CSA S304.1–04. *Design of Masonry Structures*. Mississauga, Ontario: Canadian Standard Association; 2004.
11. Ingham JM, Davidson BJ, Brammer DR, Voon KC. Testing and codification of partially grout-filled nominally-reinforced concrete masonry subjected to in-plane cyclic loads. *Masonry Society J*. 2001;19(1):83-96.
12. Voon KC, Ingham JM. Experimental in-plane shear strength investigation of reinforced concrete masonry walls. *J Struct Eng*. 2006;132(3):400-408.
13. Voon KC, Ingham JM. Experimental in-plane strength investigation of reinforced concrete masonry walls with openings. *J Struct Eng*. 2008;134(5):758-768.
14. Stavridis A, Ahmadi F, Mavros M, Shing PB, Klinger RE, McLean D. Shake-table tests of a full-scale three-story reinforced masonry shear wall structure. *J Struct Eng*. 2016;142(10):1–16, 04016074.

15. Mavros M, Ahmadi F, Shing PB, Klinger RE, McLean D, Stavridis A. Shake-table tests of a full-scale two-story shear-dominated reinforced masonry wall structure. *J Struct Eng*. 2016;142(10):1–15,04016078.

16. Koutras A, Shing PB. Shake-table test of a partially grouted reinforced masonry building with separated single grouted cells. DesignSafe-CI, DOI: https://doi.org/10.4231/D3W950P43, 2014.

17. Rajaram S, Vanniamparambil PA, Khan F, et al. Full-field deformation measurements during seismic loading of masonry buildings. *Struct Control Health Monit*. 2017;24(4):1–14,e1903.

18. Luco JE, Ozcelik O, Conte JP. Acceleration tracking performance of the UCSD-NEES shake table. *J Struct Eng*. 2010;136(5):481-490.

19. Stavridis A, Koutromanos I, Shing PB. Shake-table tests of a three-story reinforced concrete frame with masonry infill walls. *Earthq Eng Struct Dyn*. 2012;41(6):1089-1108.

20. LSTC. *LS-DYNA Theory Manual*. Livermore, CA: Livermore Software and Technology Corporation; 2018.

21. Rots JG, Blaauwendraad J. Crack models for concrete discrete or smeared? Fixed, multi-directional or rotating? *Heron*. 1989;34(1), ISSN 0046-7316.

22. Lotfi HR, Shing PB. An appraisal of smeared crack models for masonry shear wall analysis. *Comput Struct*. 1991;41(3):413-425.

23. Koutromanos I, Shing PB. Cohesive crack model to simulate the cyclic response of concrete and masonry structures. *ACI Struct J*. 2012;109(3):349-355.

24. Kottari A. *Horizontal load resisting mechanisms of external shear keys in bridge abutments*. PhD dissertation: University of California, San Diego; 2016.

25. Kim SH, Koutromanos I. Constitutive model for reinforcing steel under cyclic loading. *J Struct Eng*. 2016;142(12):1–14, 04016133.

26. Moharrami M, Koutromanos I. Finite element analysis of damage and failure of reinforced concrete members under earthquake loading. *Earthq Eng Struct Dyn*. 2017;46(15):2811-2829.

27. Murcia-Delso J, Shing PB. Bond-slip model for detailed finite-element analysis of reinforced concrete structures. *J Struct Eng*. 2015;141(4):1–10, 04014125.

28. Dulacska H. Dowel action of reinforcement crossing cracks in concrete. *ACI J Proc*. 1972;69(12):754-757.

29. Mavros M. Experimental and numerical investigation of the seismic performance of reinforced masonry structures. PhD dissertation, University of California, San Diego, 2015.

30. Kottari A, Mavros M, Murcia-Delso J, Shing PB. Interface model for bond-slip and dowel-action behavior. *ACI Struct J*. 2017;114(4):1043-1053.

31. Drysdale R, Hamid AA. *Masonry Structures Behavior and Design*. 3rd ed. The Masonry Society; 2008.

32. Mehrabi AB. Behavior of masonry-infilled reinforced concrete frames subjected to lateral loadings. PhD dissertation, University of Colorado, Boulder, 1994.

33. Bathe KJ. Conserving energy and momentum in nonlinear dynamics: a simple implicit time integration scheme. *Comput Struct*. 2007;85(7–8):437-445.